Deep Learning Enabled Label-free Cell Force Computation in Deformable Fibrous Environments

Authors: Abinash Padhi[#1], Arka Daw[#2], Medha Sawhney[2], Maahi M. Talukder[1], Atharva Agashe[1], Sohan Kale[*1,3], Anuj Karpatne[*2], Amrinder S. Nain[*1]

 # equal first authors

***corresponding authors (kale@vt.edu) (karpatne@vt.edu) (nain@vt.edu)**

Affiliations

[1]Department of Mechanical Engineering, Virginia Tech, Blacksburg, VA 24061, USA

[2]Department of Computer Science, Virginia Tech, Blacksburg, VA 24061, USA

[3]Center of Soft Matter and Biological Physics, Virginia Tech, Blacksburg, VA 24061, USA

Keywords: Cell forces, Deep learning, Mechanobiology, Cell migration, Differentiation, Nanofibers

Abstract

Through force exertion, cells actively engage with their immediate fibrous extracellular matrix (ECM) environment, causing dynamic remodeling of the environment and influencing cellular shape and contractility changes in a feedforward loop. Controlling cell shapes and quantifying the force-driven dynamic reciprocal interactions in a label-free setting is vital to understand cell behavior in fibrous environments but currently unavailable. Here, we introduce a force measurement platform termed crosshatch nanonet force microscopy (cNFM) that reveals new insights into cell shape-force coupling. Using a suspended crosshatch network of fibers capable of recovering in vivo cell shapes, we utilize deep learning methods to circumvent the fiduciary fluorescent markers required to recognize fiber intersections. Our method provides high fidelity computer reconstruction of different fiber architectures by automatically translating phase-contrast time-lapse images into synthetic fluorescent images. An inverse problem based on the nonlinear mechanics of fiber networks is formulated to match the network deformation and deformed fiber shapes to estimate the forces. We reveal an order-of-magnitude force changes associated with cell shape changes during migration, forces during cell-cell interactions and force changes as single mesenchymal stem cells undergo differentiation. Overall, deep learning methods are employed in detecting and tracking highly compliant backgrounds to develop an automatic and label-free force measurement platform to describe cell shape-force coupling in fibrous environments that cells would likely interact with in vivo.

Introduction

Contractility-driven cell migration is pivotal to many physiological processes such as wound healing, angiogenesis, tissue morphogenesis, and pathological contexts such as cancer invasion and metastasis[1,2]. During migration, cells sense several features of the fibrillar extracellular matrix (ECM), including diameter, orientation, density, stiffness, porosity, and ligand molecular composition[3]. Often, cells respond to these features by undergoing dynamic changes in the actomyosin cytoskeleton resulting in different cellular shapes and, consequently, different migration modes[4–6]. Cells interact with the fiber-rich ECM in a feedforward loop involving dynamic remodeling of the ECM, and reciprocally, the remodeled ECM impacts cell shape, contractility, signaling, and migration[7–10], and these force-based interactions remain poorly understood.

Cellular force reconstruction requires accurate measurement of the cell-induced deformation of the underlying fibrous substrate. Advanced traction force microscopy (TFM)[11–13] obtains these deformation fields through fluorescent imaging, including fluorescent, confocal, multiphoton microscopy, and second harmonic generation (SHG) microscopy[8,14–16]. A central challenge in fluorescence-based reconstruction is overcoming the harmful effects of phototoxicity and photobleaching [17–24]. On the other hand, phase-contrast microscopy's simplicity and widespread use have recently inspired deep learning-based techniques such as image-to-image translation to generate artificial fluorescent labels from phase imaging, otherwise obtained through immunochemistry labeling[17,18,20].

While numerous deep learning modules are available to track deforming structures in static backgrounds[25–27], tracking deformable structures in complex and easily deformable background environments has not been demonstrated. Here, we present a new label-free force measurement strategy using phase images capable of estimating forces of cells that undergo significant shape changes as they deform the underlying fibrous ECM resembling *in vivo* events[28,29]. Previously, we used suspended and aligned parallel fibers to measure forces exerted by elongated cells (Nanonet force microscopy (NFM))[10,30–32]. In this study, we use a crosshatch network of fibers of variable inter-fiber spacing, which we have shown to control cell migration in 1D/3D and 2D modes[33]. Specifically, dense networks of low interfiber spacing cause cells to be elongated with thicker nuclei, while those of larger spacing cause cells to be spread in 2D shapes with compressed nuclei. Our crosshatch networks match reported in vivo matrices of crossing fibers in the dermis[34,35], basement membrane[36], muscular hydrostats[37], cornea[38], and loose connective tissue[39].

We develop a deep learning-based framework to output fiber networks and track their deformations from phase contrast time-lapse movies without the need to label the fibers manually—a step that has been difficult to automate so far. The displacement fields of fiber networks are fed to a finite elements-based inverse formulation to resolve forces and contractility maps. Our label-free method, termed crosshatch Nanonet Force Microscopy (cNFM), alleviates the need for fluorescent fiduciary markers ubiquitously used in other force measurement methods, thus allowing us to estimate the force signatures of cells over extended times (~weeks). We observe an unexpected order-of-magnitude drop in forces as migratory cells change shapes and report forces required to differentiate mesenchymal stem cells into adipogenic and osteogenic lineages. Overall, we address a long-standing mechanobiological need in linking cell shape and fibrous ECM deformation through contractility, with implications for physiological and pathophysiological conditions.

Results

Framework to compute cellular forces from phase contrast images

A central challenge in accurately capturing fiber network deformation arises from their occlusion by the cell body. As human-mesenchymal stem cells (hMSCs) migrate on fibrous ECM, they significantly deform the underlying fiber network by applying contractile forces (**Fig. 1A**, **Supplementary movie M1**). While fluorescently tagging the fibers can facilitate their observation, prolonged fluorescent imaging can affect cellular behavior[21–24]. To overcome this limitation, we developed a deep learning-based pix2pix model that can reveal fiber grids in phase contrast images without the need for fluorescent imaging (**Fig. 1Bi**). We trained our pix2pix model using sets of paired phase and fluorescent images. Once trained, our model can generate synthetic fluorescent images of fiber networks from experimental phase images. To measure the displacement fields in the fiber grids from the synthetically generated fluorescent images, we first utilize a deep learning-based object detection module to identify the node intersections of the grids in each fluorescent image. The grid intersections serve as natural fiduciary markers. We then apply a bi-directional node-tracking algorithm to track every node intersection across all frames using information from past and the future frames (**Fig. 1Bii**). The displacement fields computed from the grid intersections and the overall fiber shapes in the synthetic fluorescent images are used as inputs in the inverse problem formulation to reconstruct force fields (**Fig.1C**).

Extracting the deformed fiber grid using pix2pix deep learning module

Our framework's first step is automatically recreating fiber networks from experimental phase contrast images. To achieve this, we developed a pix2pix model[40] (**Fig. 2Ai**) that belongs to the class of deep learning models referred to as conditional Generative Adversarial Networks (cGANs)[41,42]. cGANs comprise of two neural network models, a generator, G, and a discriminator, D. The generator learns a mapping from the input image x (phase contrast images) to the real output image y (experimental or "real" fluorescent images), $G: x \rightarrow y$, while the discriminator tries to distinguish between "real" outputs and synthetically generated outputs ("fake" fluorescent images $G(x)$). We trained our pix2pix model using a manually curated data set of phase contrast and fluorescent image-pairs (refer to **Supplementary Note 1** for more details on dataset generation). Once trained, our pix2pix model robustly and automatically generates fluorescent images of deformed fiber networks from experimental phase contrast images (**Fig. 2Aii, Supplementary movies M2, M3**).

Fiber-network displacement field extraction from fiber grid deformations

We next sought to track the force-induced deformations in the fiber networks from the generated fluorescent images. Using network grid intersection points as fiduciary markers, we extracted the nodal coordinates across all frames by using a deep learning-based object detection module followed by a bi-directional node-tracking algorithm. In particular, we used *RetinaNet*[43] (**Fig. 2Bi**), a commonly used object detection model in computer vision, to detect grid intersections/nodes (shown as red dots). We trained our *RetinaNet* on a labeled set of synthetic fluorescent images, where every image was tagged with its corresponding node annotations. Once trained, the *RetinaNet* predicts a set of bounding boxes likely to contain a grid intersection/node and a confidence score (between 0 and 1) for every predicted bounding box. Any bounding box with a confidence score greater than 0.7 was considered a detected node.

We found that while *RetinaNet* was able to detect most of the nodes, some of the nodes were still being missed as *RetinaNet* only uses information from the current frame and does not consider the information of previous and future frames. To address this limitation, we developed a bi-directional tracking algorithm to identify missing nodes comprising of two tracking steps. First, we apply the *Cross-correlation* module that is part of the *forward node* tracking algorithm (**Fig. 2Bii**), which uses the positions of detected nodes in the previous frame (*t-1*) and propagates it forward in time to fill in the missing nodes of the current frame (*t*, shown as green triangles). The candidate

cross-correlated nodes were then combined with the detected nodes from *RetinaNet* at frame *t* using a *Matching* algorithm (see **Fig. S4** for details on the cross-correlation and matching modules). This step allows recovery of missing nodes at time *t* that were detected in previous frames. In the second step, we consider the goal of recovering missing nodes at frame *t* that were detected in future frames. To achieve this goal, we applied our tracking algorithm in the backward direction, resulting in the complete bi-directional tracking algorithm (**Fig. 2Biii** and see materials and methods for details on the bi-directional tracking algorithm). Nodes recovered from the backward pass at time *t-1* using detected nodes at time *t* are shown as yellow diamonds. This strategy allowed us to generate artificial fiber networks with an accurate description of nodes at each time point.

Next, we determined our approach's effectiveness using two quantitative evaluation metrics[44]: *Precision* and *Recall*. *Precision* is defined as the ratio of the number of nodes correctly identified by the algorithm to the total number of nodes predicted by the algorithm in the synthetically generated images. On the other hand, *Recall* is defined as the ratio of the number of nodes correctly identified by the algorithm to the actual number of nodes present in the ground truth. Thus, for an ideal model, *Precision* and *Recall* should equal 1. We analyzed seventeen videos (**Fig. 2Biv**) and found the *Precision* and *Recall* to be ~1, thus demonstrating that the performance of our node detection and tracking modules is very close to ideal performance. To evaluate the spatial accuracy of tracked fiber intersections, we defined the average root mean squared error (RMSE) of a tracked node as the Euclidean distance between node coordinates in the actual experimental image and the prediction of our tracking module. Smaller values of RMSE reflect high spatial accuracy in identifying the fiber intersection. The distribution of the RMSE (of nodes in every frame of a video) is shown in **Fig. 2Bv**. We found that the average nodal error is less than 2 pixels, which is comparable to the human errors in measurements. We also compared the Node Detection Score (the confidence score generated by *RetinaNet*) and the RMSE across all detected nodes (44,852 in number) using a scatter plot (**Fig. 2Bvi**), where the colors are proportional to the probability density function of points in the scatter plot. We can see that the RMSE is small for majority of detected nodes with high confidence scores (greater than 0.7), further validating our decision to eliminate detected nodes with confidence less than 0.7. Overall, we present a quantitative strategy utilizing a combination of image-to-image translation, node detection, and node tracking that robustly allows us to track fiber intersections in the continuously deforming networks. Nodal displacements were then measured against a reference grid, generated artificially by leveraging the uniform geometry of crosshatch fiber networks and connecting the boundary nodes in the region of interest (**Supplementary Note 2, Fig. S5**).

Error analysis of forces estimated by the inverse formulation

Next, we developed an inverse formulation to infer forces from the nodal displacements and deformed fiber shapes (see Methods). To validate our inverse formulation and test the accuracy of the recovered forces, we generated nodal displacement data ($\boldsymbol{u}_m$) at grid intersections by applying representative force patterns on the computational nanonet (red arrows in **Fig. 3A**). We simulated the measurement errors in nodal displacements (**Fig. S4**) by adding a zero-mean Gaussian noise of varying strength σ_e = {0.0 μm, 0.1 μm, 0.2 μm, 0.5 μm} to $\boldsymbol{u}_m$. An example of the recovered force pattern obtained by solving the regularized inverse problem for σ_e = 0.2 μm is shown in **Fig. 3A** with green arrows. The contractile force pattern is recovered to within 10% of the applied force pattern (**Fig. 3Bii**), where the forces are compared after summing within a circular patch of 20 μm in radius. We find that averaged measurements of the force patterns (overall contractility C, see Methods) are recovered with even higher accuracy than the pointwise comparison of expected and recovered force patterns (**Supplementary Note 3**). The regularization parameter β (*i.e.,* penalty parameter to avoid large unphysical forces in the inverse solution) is chosen based on the L-curve (**Fig. 3Bi**), where the magnitude of reconstructed forces

$||\mathbf{t}||$ is plotted as a function of the normalized matching errors for a range of β values. On a typical L-curve, a sharp increase in $||\mathbf{t}||$ is observed as β approaches zero because of overfitting the solution to the noise in measured data. This feature is missing in our L-curves due to the image-based fitting term, which inherently avoids large forces by constraining nanonet deformations to the fluorescent fiber shapes. The vertical dotted lines shown in (**Fig. 3Bi**) denote the level of noise σ_e , measured in the nodal displacements. The inverse solver reduces the normalized matching errors within this noise level (see **Supplementary note 3** for detailed analysis and more validation examples).

Next, having validated our inverse methods, we extracted the forces of cells moving on fiber networks. Starting from a phase contrast image from experiments, we used our machine learning pipeline (**Fig. 2**) to generate a fluorescent image to calculate nodal deformations required for calculating cell forces (**Fig. S5, S6**). The magnitude of the nodal forces obtained depends upon the length of the finite elements used to discretize the nanofibers. To avoid mesh resolution dependency, we report the force in line tension (value obtained by dividing the force with the element length in units of mN/m, or equivalently nN/μm, **Fig. S6C**). We observe line tensions in the range 5-25 mN/m, which over a representative adhesion patch on fibers of 10 μm results in 50-250 nN force, in agreement with forces reported by our parallel-fiber network based Nanonet Force Microscopy[45]. The typical force per adhesion patch is measured to be in a similar range using soft gels (2-50 nN[46,47]), fibrous networks (100-400 nN[31,45]), and micropost arrays (1-80 nN[46,48,49]). To visualize the spatial organization of cellular contractility, we developed force polarity maps that show the contractility C_θ at an angle θ to the *x*-axis in a polar plot (**Fig. S6D**, methods). Overall, the inverse formulation accurately assesses the cellular contractility and force distribution from the measured nodal deformations.

Cellular contractility in dynamic ECM interactions and stem cell differentiation

Having achieved high fidelity in the automatic reconstruction of deformed fiber networks, next, we wanted to test our platform's sensitivity and robustness in determining cellular contractility. First, we confirmed that our platform captured the loss and gain of contractility in cells treated with pharmacological inhibitors. As cytoskeletal elements are central to cellular polarity and contractility, we wanted to test the role of actin, one of the major components of cellular makeup. Pharmacological inhibition of actin with Latrunculin B showed a reduction in forces compared to the control condition (**Fig. 3C, Supplementary movie M4**). We also tested the loss of contractility through pharmacological inhibition of ROCK (Rho-associated kinase, another key player in cellular contractility) using the drug Y-27632. As expected, the pharmacological inhibition reduced the forces within 30 min (**Fig. 3Di, ii, Supplementary movie M5**). Washing out the drug caused the cells to re-establish force polarity to pre-inhibition forces (**Fig. 3Diii, iv**).

Next, we inquired how contractility varied as cells migrated and changed shapes in the dynamic ECM environment. Previously, we have demonstrated the ability to control cell shapes and migration direction within the same scaffold through the design of interfiber spacing in crosshatch networks[33]. To understand anisotropic shape cell forces, we selected fiber geometry of crosshatch fiber networks of 25 μm X 8 μm (rectangular grids, **Fig. 3E, Supplementary movie M6**). We found that forces exerted by cells in elongated morphology along rectangular grids are mainly concentrated at the leading and trailing ends of the cell body (**Fig. 3Ei-iii**). Force polarity maps confirmed the forces in the cell transverse direction to be lower than those along the fibers (**Fig. 3Eiv**), in agreement with the patterns observed in polarized cell migration[50,51]. We next generated hybrid fiber networks of a square region (30 μm X 30 μm) transitioning into rectangular regions (30 μm X 15 μm), forcing cells to be in the spread and elongated shapes, respectively (**Fig. 4A, Supplementary movie M7**). We tracked the contractility values and observed that as the cells migrated across regions, the migration cycle entailed low and high contractility. Selected time

points are annotated on the contractility plot, and their corresponding line tension plots are shown. Unexpectedly, cells transitioned from high forces (spread morphologies) to an order-of-magnitude reduction as they transitioned to elongated shapes. The total contractility of hMSCs has been reported to be in a similar magnitude range on PDMS micropost arrays (~1000nN[52] and 1000-5000nN[46] depending on cell area) and on polyacrylamide gels (~600-6000nN[53] depending on substrate stiffness), and here, we show how the forces change with cell shape and migration. We further investigated the capacity of the proposed framework to resolve forces between interacting cells on nanonets (**Fig. 4B** and **Supplementary movie M8**). The contractility of both cells cycled between high and low values corresponding to different shapes during migration.

Finally, we addressed the long-standing gap in understanding how contractility-driven stem cell differentiation occurs in compliant fibrous environments. Stem cell fate is influenced by matrix elasticity in non-degradable matrices[54], while in degradable matrices, traction forces play a significant role[55]. Though traction forces in differentiating cells have been studied before[46,55,56], how the forces evolve in compliant fibrous ECM has yet to be reported. We investigated how forces evolve as stem cells commit to adipogenic and osteogenic lineages. We treated hMSCs with adipogenic differentiation medium and osteogenic medium for nine days. The representative images show nanonet deflections as differentiation progressed (red box for adipogenic differentiation in **Fig. 4Ci** and blue box for osteogenic differentiation in **Fig. 4Cii**). We measured the cell forces across different days and observed that cells differentiating toward adipogenic lineage exerted lower forces, and cells differentiating toward osteogenic lineage exerted higher forces compared to the control group comprising cells in a growth medium (**Fig. 4Ciii**). We confirmed differentiation by staining for lipid droplets (adipogenic) using Oil Red (Fig. 4Ci, **Fig. S20**) and alkaline phosphatase activity (ALP for osteogenic, Fig. 4Cii, **Fig. S21**). Overall, we demonstrate our platform's robustness to estimate single cell contractility in a variety of biological conditions, including cell-cell interactions, response to drugs, migration in different shapes, and differentiation.

Discussion

We present a new automated and label-free approach using suspended crosshatch nanonets of varying interfiber spacing for calculating cell forces. By controlling the fiber architecture, the cell shape is regulated, and the force polarity is determined. We can measure the fiber deformations without fiduciary fluorescent markers by using deep learning methods to automatically generate the fluorescent equivalent images of fiber networks from phase contrast microscopy. Our method eliminates the harmful effects of phototoxicity and photobleaching, thus allowing us to calculate forces over longer timescales in dynamically changing fibrous environments mimicking the native ECM. Further, training our deep learning routines using a pristine set of phase images eliminates artifacts usually associated with fluorescent imaging, such as blurriness, non-uniform intensity and background noise (discussed further in **Supplementary Note 1**).

Existing force resolution algorithms are not directly applicable for the nanonets as most TFM approaches are based on a continuum representation of the substrate in 2D/3D. In contrast, nanonets are discrete grids made up of slender structural elements. The force reconstruction inverse formulation is robust in noisy environments of significantly deformed fiber shapes. The cellular contractility computed agrees with previously reported values from other established force measurement platforms[52,53,56–58]. Unexpectedly, our measurements reveal that during cell migration, the forces can change by order of magnitude that coincides with cell shape changes. Thus, cNFM serves as a versatile platform allowing analysis of the same cell undergoing different biophysical states based on changes in the design of the fiber matrix or made by the cell to the fiber matrix.

While successfully estimating cell forces in deformable environments, our proposed force computation pipeline has a few cautionary constraints. First, the precision of our pix2pix model may be limited when generating fiber profiles underneath fully opaque cells that occlude the background fiber grids. Second, the current strategy to extract network deformations involves estimating the undeformed network shape by fitting straight lines to the deformed network (**Supplementary Note 3**). This approach works well when the cell is close to the center of the imaging frame, enabling selecting points around the cell to fit a reference grid of straight lines. However, our strategy eliminates the need for cell removal through trypsinization for reference generation commonly employed in other methods[47,59,60]. Thirdly, the inverse formulation is not applicable if plastic deformations are induced in the network. However, the pretension provides a sufficient buffer that ensures elastic response except for exceptionally high contractile forces (>1000 nN per adhesion patch). Finally, rare non-planar network deformations are still possible if cells generate out-of-plane forces or if nanofibers buckle out-of-plane under compressive in-plane contractile forces.

In conclusion, we present a new fiber-based cell-force computation technique in which the complex fiber architecture is reproduced using deep learning. By varying the arrangement of crosshatch fibers, we control the cell shapes and the associated force polarity in migration, thus providing the ability to interrogate force feedback loops in cell-fiber force and shape coupling. Our method takes advantage of fiber networks of controlled-architecture to resolve force fields using inverse formulation in a label-free method without the need to tag the environment or fibers fluorescently. In the future, we envision that our platform using contextual and tunable fiber networks will allow the precise study of the force feed loops in multiple physiological and pathophysiological applications.

Materials and Methods

Nanonet manufacturing

The suspended crosshatch fiber networks were generated using previously reported non-electrospinning STEP technique[61–63]. Briefly, suspended ~250nm fibers were spun out of Polystyrene (Scientific Polymer, NY) dissolved in Xylene (Thermofisher) solution in two orthogonal layers. Different interfiber spacings were tested and the most commonly used was ~25μm (both directions). The rectangular patterned fiber scaffolds had ~25μm in X-direction and 5-8μm in Y-direction.

Cell culture and imaging

Human mesenchymal stem cells (hMSCs, Lonza) were cultured on fiber scaffolds (for training data set generation, treatment with rhodamine tagged fibronectin (Cytoskeleton Inc, CO)) in 5% CO2 and 37°C. All imaging was performed in Zeiss AxioObserver Z1 with 20x objective. See **Supplementary Note 4** for details on differentiation media composition, protocols for Oil Red O, ALP staining and semi-quantitative analysis of the obtained RGB images (with camera Amscope MU300).

Phase to fluorescent image translation using pix2pix

We used a pix2pix model to translate the phase contrast images to fluorescent images. Details of the pix2pix model are provided in the **Supplementary Note 1**. Our pix2pix model was trained on a pristine set of phase and fluorescent image pairs. Please refer to the **Supplementary Note 1** for additional details on the training/testing setup as well as the dataset generation procedure.

Node detection and tracking

We used *RetinaNet* to detect grid intersections from the synthetically generated fluorescent images. Additional details of *RetinaNet* are provided in the **Supplementary Note 1**. We further developed a bi-directional tracking algorithm to recover nodes that were not detected by the *RetinaNet*. Specifically, the tracking algorithm utilized information from the previous and future frames to recover nodes at a current frame. More details on the bi-directional tracking algorithm and the training and testing setups of node detection and tracking are provided in the **Supplementary Note 1**.

Finite elements (FE) based inverse formulation of cNFM

The nanofibers are modeled as beams undergoing elastic deformations with significant pretension arising from the manufacturing process[31]. For the FE model of nanofibers mechanics, we used corotational beam formulation[64] that accounts for the geometrical nonlinearities due to large rigid body motions and small elastic strains in a corotating frame. The inverse problem is formulated as a regularization-based minimization problem constrained by the nanonet mechanics. The formulation is therefore similar in structure to classical traction force microscopy on soft gels[50,65]. The inverse problem solver attempts to minimize the difference between measured and FE model deformations by tweaking the unknown nodal forces. The difference is quantitated using an error function with two contributions: (1) difference between nodal displacements at grid intersections in measured data and the FE model, and (2) misalignment between deformed fiber shapes in artificial fluorescent images and the FE model, similar to the active-contour segmentation approach[66,67]. Furthermore, a regularization term penalizes the magnitude of nodal forces to avoid overfitting the noise in measurements. We perform the minimization of the objective function (error + regularization) using the Broyden–Fletcher–Goldfarb–Shanno (BFGS) algorithm[68] where the gradient of the nonlinear implicitly-constrained minimization problem is obtained by using the adjoint-set method[69–71]. The details of our inverse formulation, finite elemental model, and validation are provided in **Supplementary Note 3**.

Contractility and force polarity maps

The estimated force pattern $\mathbf{t}$ is obtained as a set of nodal forces on the computational finite elemental mesh. To quantitate $\mathbf{t}$, we extract the overall cell contractility as a biophysical measure of cell mechanics defined as[50]

$$C = \sum_I \frac{\mathbf{t}_I \cdot (\boldsymbol{x}_I - \boldsymbol{r}_c)}{|\boldsymbol{x}_I - \boldsymbol{r}_c|}$$

where $\mathbf{t}_I$ is the estimated force at node I, $\boldsymbol{x}_I$ is the position vector of that node, and $\boldsymbol{r}_c$ is the epicenter of the force pattern. The epicenter of the force pattern is defined as a point that minimizes the sum of cross-products of nodal force vectors with the position vector from the epicenter such that $\boldsymbol{r}_c = \underset{\mathbf{r}}{\operatorname{argmin}}\, W_c(\boldsymbol{r})$, where $W_c(\boldsymbol{r}) = \sum_I |\mathbf{t}_I \times (\boldsymbol{x}_I - \boldsymbol{r})|$.

Furthermore, the orientational organization of the force pattern is examined by evaluating the polar distribution of cellular contractility using

$$C_\theta = \sum_I t_{\theta,I} \boldsymbol{e}_\theta \cdot \frac{(\boldsymbol{r}_c - \boldsymbol{x}_I)}{|\boldsymbol{r}_c - \boldsymbol{x}_I|},$$

where $\boldsymbol{e}_\theta$ is a unit vector at an angle θ to the x-axis and $t_{\theta,I} = \min(\mathbf{t}_I \cdot \boldsymbol{e}_\theta, 0)$. For a contractile force pattern, C_θ quantifies the contractility along $\boldsymbol{e}_\theta$. The force polarity map is then obtained by plotting C_θ in polar coordinates (Fig. 3C-E iv). This map visually reveals any preferential alignment of contractile forces along a given direction.

Acknowledgements ASN, SK, and AK acknowledge funding support from National Science Foundation (NSF, Grant No. 2107332). ASN acknowledges the Institute of Critical Technologies and Science (ICTAS) and Macromolecules Innovative Institute (MII) at Virginia Tech for their support in conducting this study.

Author contributions. ASN conceived and supervised the research. AP, AD, SK, AK, and ASN designed experiments. AD, MS, and AK developed the machine learning algorithms. SK developed the analytical and computational model. AP and AA ran experiments. AP, MMT, and SK ran simulations. All authors analyzed data. AP, AD, MS, and SK wrote the manuscript. All authors edited the manuscript.

List of Supplementary Movies

1. **Supplementary Movie M1**: **Significant fiber deformations by contractile migrating hMSCs** Time lapse of phase contrast images showing migrating human mesenchymal stem cells (hMSCs) and the corresponding fluorescent images of rhodamine tagged fibers being significantly deformed under contractile forces.
2. **Supplementary Movie M2**: **Trained pix2pix model output** Time lapse of migrating hMSCs on deforming fibers showing phase-contrast image (left), experimentally obtained fluorescent images or ground truth (center) and the output from trained pix2pix model (right). Pix2pix generated images are devoid of the aberrations observed in the ground truth fluorescent images
3. **Supplementary Movie M3**: **Trained pix2pix model output** Time lapse of migrating hMSCs on deforming fibers showing phase-contrast image (left), experimentally obtained fluorescent images or ground truth (center) and the output from trained pix2pix model (right). Pix2pix generated images are devoid of the aberrations observed in the ground truth fluorescent images
4. **Supplementary Movie M4**: **Actin-dependent force dynamics** Line tension map and corresponding force polarity maps depicting higher contractility of cells in control condition and significantly reduced contractility when treated with actin inhibitor latrunculin B. Scale bar: white bar: 50μm green arrow: 35mN/m
5. **Supplementary Movie M5**: **ROCK pathway dictates cellular contractile dynamics** Line tension map and corresponding force polarity maps depicting higher contractility of cells in control condition and significantly reduced contractility when treated with ROCK inhibitor Y27632. Contractility is regained when drug is washed off. Scale bar: white bar: 50μm green arrow: 35mN/m
6. **Supplementary Movie M6**: **Rectangular fiber arrangement causes cellular anisotropy** Line tension map and corresponding force polarity maps shows anisotropic cell shapes and polarized migration along rectangular crosshatch fiber arrangements Scale bar: white bar: 50μm green arrow: 35mN/m
7. **Supplementary Movie M7**: **Hybrid fiber architecture dictates varied cellular shape and contractility** Line tension map and corresponding force polarity maps shows varied cell shapes and cycles of low and high contractility as the cell migrates from a sparse

region to a denser arrangement of fibers, accompanied with a drastic drop in the contractility by an order of magnitude. Scale bar: white bar: 50μm green arrow: 35mN/m

8. **Supplementary Movie M8**: **Force dynamics of multiple interacting cells** Line tension map and corresponding force polarity maps shows two initially interacting cells and the emergence of third interacting cell through mitosis as all of them move apart. Scale bar: white bar: 50μm green arrow: 35mN/m

Figures and Tables

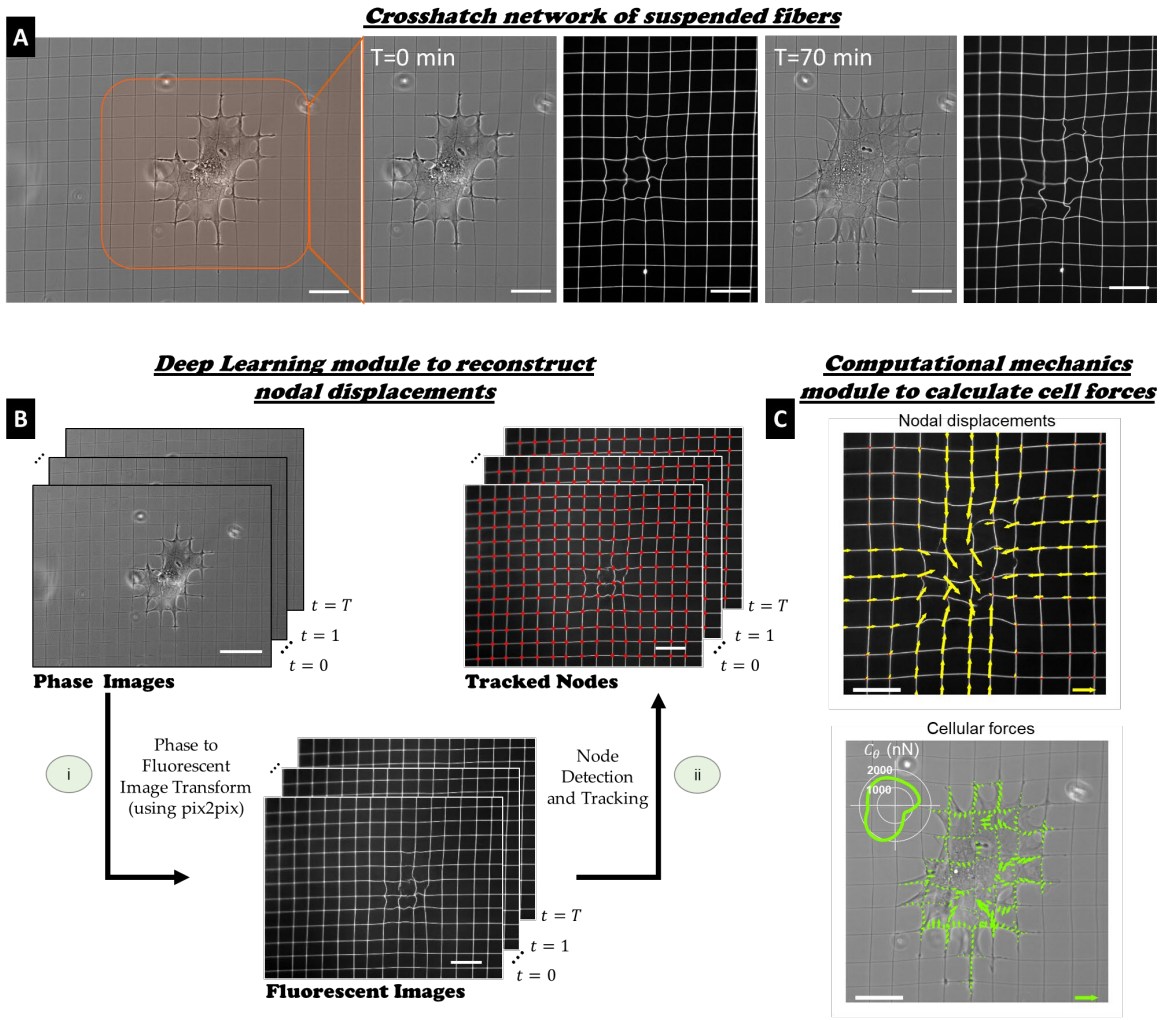

Figure 1. **Schematic pipeline for cellular force computation.** (A) Suspended crosshatch fiber networks are generated using non-electrospinning STEP technique. Cells migrate in different shapes while deforming the underlying fiber network, as seen in experimentally obtained phase as well as fluorescent images. Experimental fluorescent images are used exclusively for training the deep learning modules. (B)(i) Experimentally obtained phase images are transformed into synthetically generated fluorescent images through deep learning-based pix2pix model. (ii) Using a deep learning based object detection model *RetinaNet* followed by a bi-directional tracking algorithm, the nodal intersection points of the fiber network are identified (shown as large red dots for visualization purposes). (C) Displacement fields are calculated using the extracted nodal points (yellow arrows). Cellular forces are computed from obtained displacement fields and are represented as line tension (green arrows). Force polarity map C_θ (inset) captures the orientational distribution of cellular forces. Scale bars: 50µm, Yellow arrow: 5µm, Green arrow: 35 mN/m

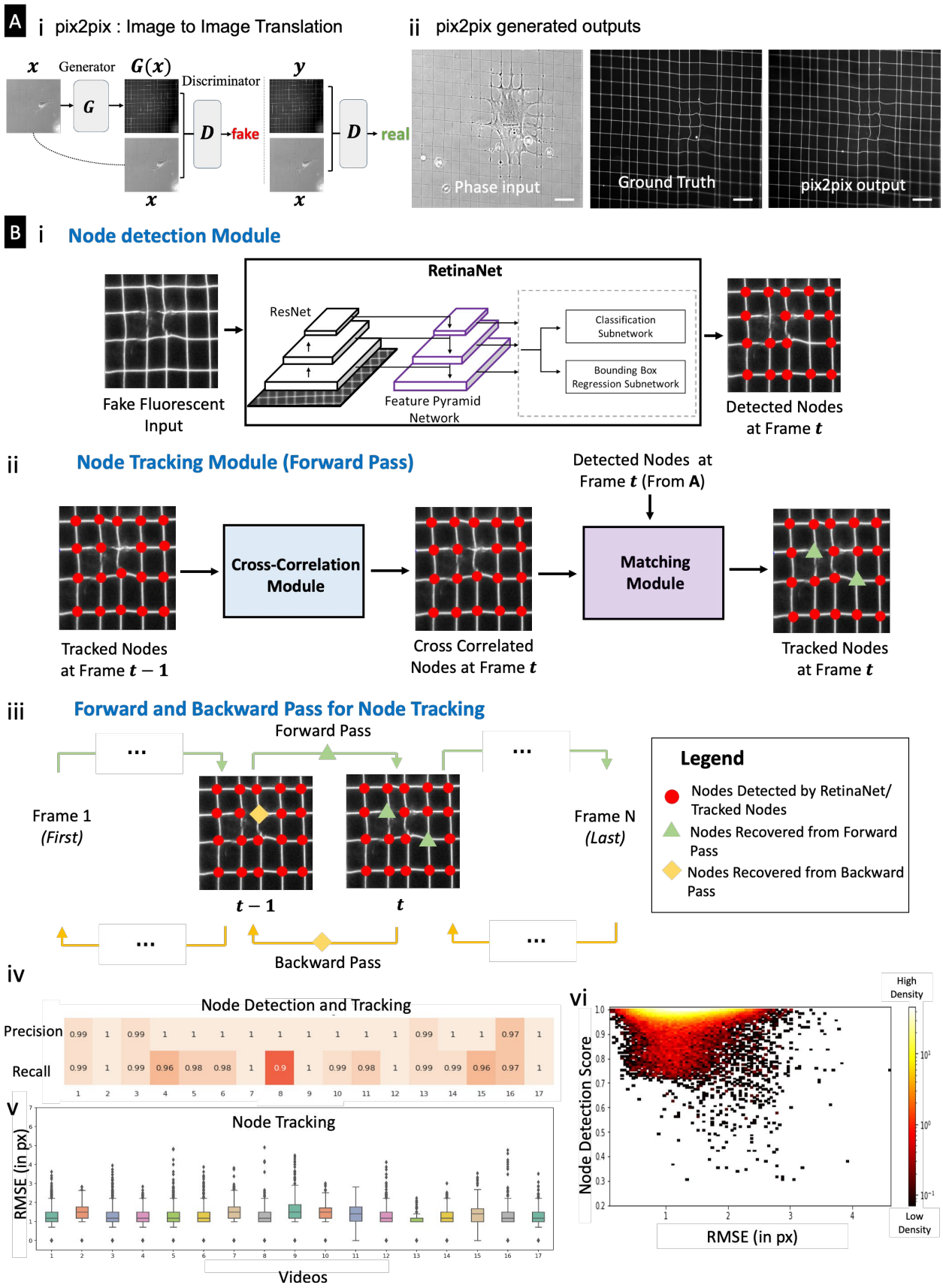
A
i pix2pix : Image to Image Translation
ii pix2pix generated outputs
x
Generator
G(x)
G
Discriminator
D
fake
y
D
real
x
x
Phase input
Ground Truth
pix2pix output
B
i Node detection Module
Fake Fluorescent Input
RetinaNet
ResNet
Feature Pyramid Network
Classification Subnetwork
Bounding Box Regression Subnetwork
Detected Nodes at Frame t
ii Node Tracking Module (Forward Pass)
Detected Nodes at Frame t (From A)
Tracked Nodes at Frame t − 1
Cross-Correlation Module
Cross Correlated Nodes at Frame t
Matching Module
Tracked Nodes at Frame t
iii Forward and Backward Pass for Node Tracking
Forward Pass
Frame 1 (First)
Frame N (Last)
t − 1
t
Backward Pass
Legend
Nodes Detected by RetinaNet/ Tracked Nodes
Nodes Recovered from Forward Pass
Nodes Recovered from Backward Pass
iv
Node Detection and Tracking
Precision
Recall
v
Node Tracking
RMSE (in px)
Videos
vi
Node Detection Score
RMSE (in px)
High Density
Low Density

Figure 2. Deep-learning based image reconstruction and feature extraction (A) (i) Schematic representation of our proposed pix2pix model which generates fluorescent images from input phase contrast experimental images (ii) A test example of a synthetically generated fluorescent image obtained from a trained pix2pix model. Scale bar: 50 μm (B) (i) Node Detection Module that uses a deep-learning based object detection model called *RetinaNet* to identify grid intersections/nodes from synthetically generated fluorescent images. (ii) An illustration of the forward pass of the node tracking algorithm, (iii) A schematic representation of the forward and backward passes of the proposed bi-directional Tracking algorithm, (iv) *Precision* and *Recall* values of the predicted nodes after node detectoin and tracking are close to ~1 across all 17 videos, indicating close to ideal performance. (v) The distribution of Nodal Errors observed after node detection and tracking in each video shows that the average nodal error is less than 2 pixels, which is comparable to human error in measurements, (vi) The scatter plot of node detection confidence scores vs nodal errors shows high confidence (greater than 0.7) of the RetinaNet for majority of the predicted nodes with low nodal errors.

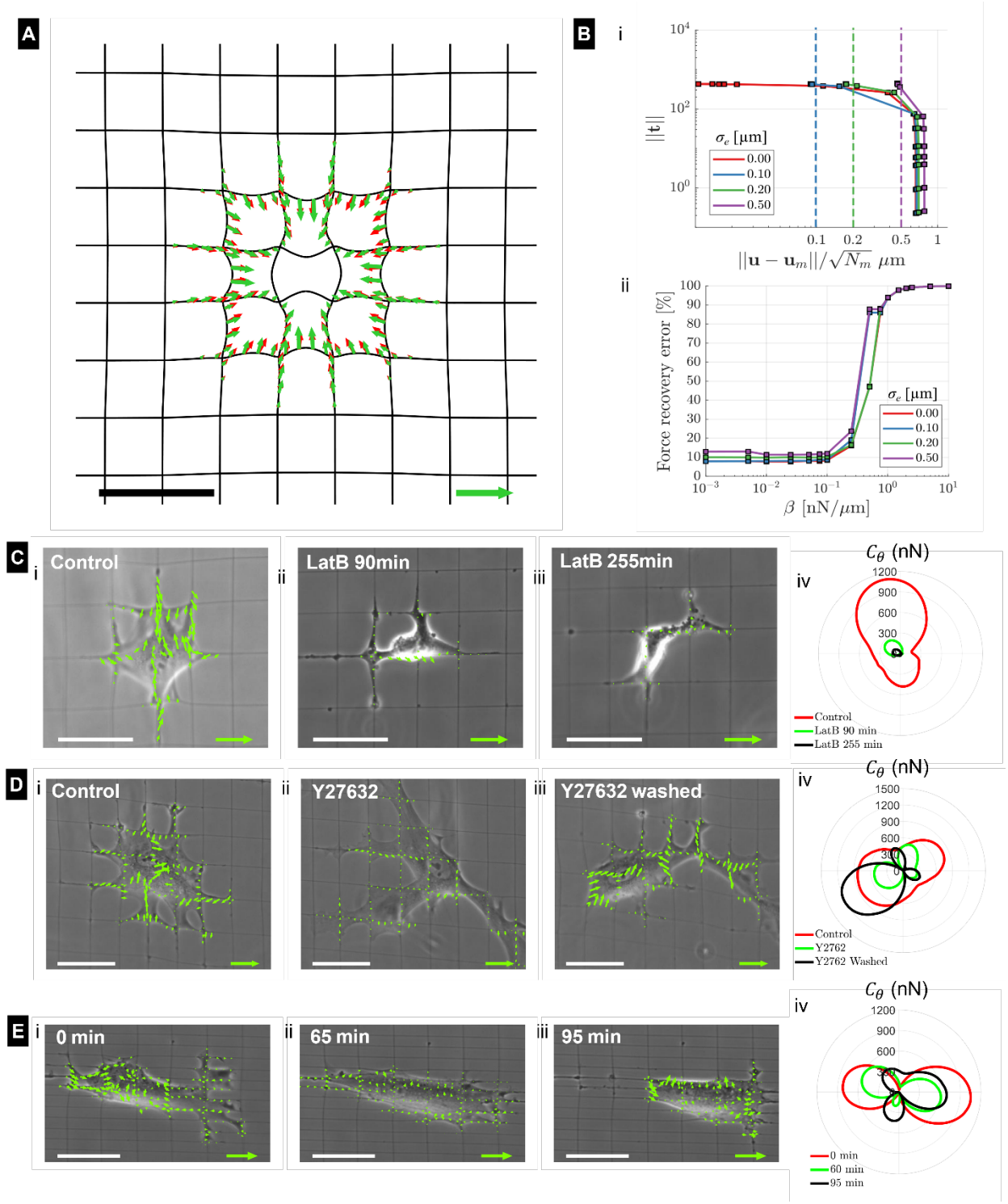

Figure 3. **Inverse formulation to estimate forces on crosshatched nanofiber networks.** (A) An example of validation of the inverse formulation with a representative radial contractile force pattern (red arrows) generateing the displacements $\boldsymbol{u}_m$ at grid intersections. The inverse problem is solved using $\boldsymbol{u}_m$ with zero-mean Gaussian noise of standard deviation σ_e. The solution obtained for a typical noise strength $\sigma_e = 0.2$ μm is shown with green arrows. (B) Analysis of the validation example in (A) for different σ_e. (i) The L-curves showing magnitude of the force pattern $||\mathbf{t}||$ as a

function of the displacement matching error $||\mathbf{u} - \mathbf{u}_m||$ normalized by the number of measured nodes N_m for a range of regularization parameter β from 10 to 10^{-3} nN/μm. (ii) Recovery of forces as a function of β for different σ_e. The forces are compared after summing up within a patch of 20 μm radius (see Supplementary Note 3). (C) Line tension map of cell (i) under control condition, presence of Latrunculin B (actin inhibitor) after (ii) 90min, and (iii) 255min. (iv) Force polarity maps capturing the orientational distribution of cellular forces. (D) Line tension map of cell (i) under control condition, (ii) in presence of Y27632 drug (ROCK inhibitor), and (iii) after drug wash off showing contractility recovery. iv. Force polarity maps for cases i-iii. (E) i-iii. Line tension map of cells migrating in aligned morphology on rectangular crosshatch fibers tracked over tens of minutes. iv. Force polarity maps capturing the horizontal alignment of cellular forces. Green tension scale arrow: (A) 25 mN/m, (C-E) 35 mN/m. Black/White scale bars: (A, C-E) 50 μm.

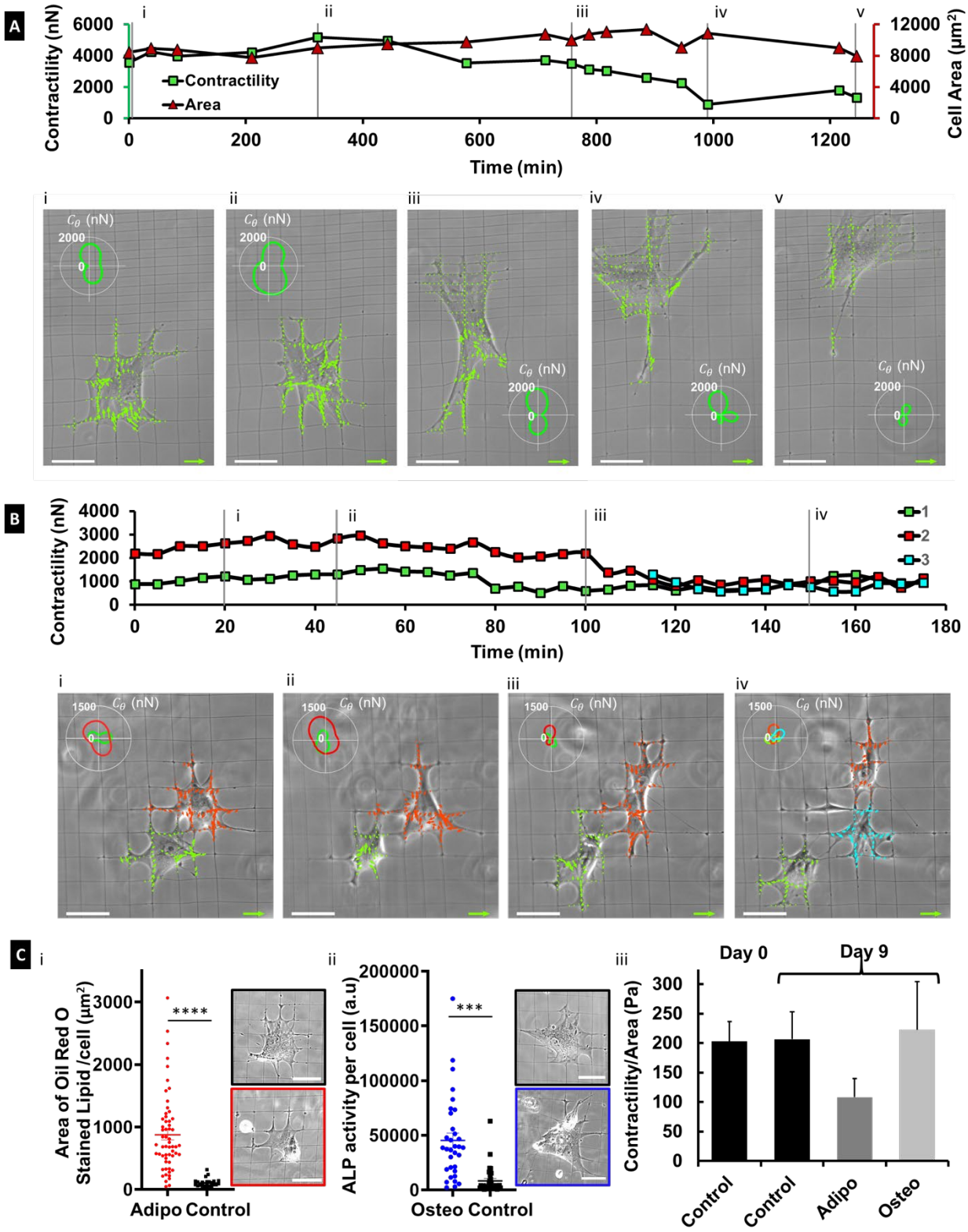

Figure 4. Forces in shape-controlled cell migration, cell interactions, and stem cell differentiation. (A) A single cell exerts cycles of low and high contractility across the migration

cycle as it transitions through different shapes. Line tension maps are shown for times marked as i-v of the cell migrating across regions of different fiber arrangements in different shapes. Force polarity maps C_θ (insets) capture the change of force polarity with cell morphology and motion. (B) Time evolution of contractility of two interacting cells and line tension maps for selected frames i-iv. Force polarity maps C_θ (insets) depict the evolution of the force patterns of interacting cells along the direction of respective cell motion. (C) i. Total area covered by Oil Red O stained lipid droplets quantified for cells treated with adipogenic medium vs growth medium (control) confirms adipogenic differentiation. n=58(N=5) for Adipogenic, n=25(N=2) for Control. Image in black box represents cell on Day0 and image in red box is of a cell on Day9. ii. Alkaline phosphatase (ALP) activity of cells in osteogenic medium vs growth medium (control) expressed in arbitrary units indicate osteogenic differentiation. n=33(N=4) for Osteogenic, n=32(N=2) for Control. Image in black box represents cell on Day0 and image in blue box is of a cell on Day9. iii. Cells in growth medium (control) maintain contractility magnitudes over 9 days. Cells undergoing adipogenic differentiation exhibit lower contractility than both cells in growth medium (control) and cells undergoing osteogenic differentiation. n=15(N=2) for Control Day-0, n=10(N=5) for Adipogenic, n=6(N=4) for Osteogenic and Control Day-9. n=number of cells, N=number of independent samples (2 sets of independent experiments were performed for all the data) Green tension scale arrow: (A, B) 35 mN/m. White scale bar: (A, B) 50μm.

1. Lauffenburger, D. A. & Horwitz, A. F. Cell migration: a physically integrated molecular process. *Cell* **84**, 359–369 (1996).

2. Ananthakrishnan, R. & Ehrlicher, A. The forces behind cell movement. *Int. J. Biol. Sci.* **3**, 303–317 (2007).

3. Emon, B. *et al.* A novel method for sensor-based quantification of single/multi-cellular traction dynamics and remodeling in 3D matrices. *Sci. Adv.* 35–39 (2020). doi:10.1101/2020.09.24.311647

4. Grinnell, F. Fibroblast mechanics in three-dimensional collagen matrices. *J. Bodyw. Mov. Ther.* **12**, 191–193 (2008).

5. Friedl, P. & Wolf, K. Plasticity of cell migration: A multiscale tuning model. *J. Cell Biol.* **188**, 11–19 (2010).

6. Alt-Holland, A. *et al.* E-cadherin suppression directs cytoskeletal rearrangement and intraepithelial tumor cell migration in 3D human skin equivalents. *J. Invest. Dermatol.* **128**, 2498–2507 (2008).

7. Malik, R., Lelkes, P. I. & Cukierman, E. Biomechanical and biochemical remodeling of stromal extracellular matrix in cancer. *Trends Biotechnol.* **33**, 230–236 (2015).

8. Cox, T. R. & Erler, J. T. Remodeling and homeostasis of the extracellular matrix: Implications for fibrotic diseases and cancer. *DMM Dis. Model. Mech.* **4**, 165–178 (2011).

9. Larsen, M., Artym, V. V., Green, J. A. & Yamada, K. M. The matrix reorganized: extracellular matrix remodeling and integrin signaling. *Curr. Opin. Cell Biol.* **18**, 463–471 (2006).

10. Padhi, A. *et al.* Force-exerting perpendicular lateral protrusions in fibroblastic cell contraction. *Commun. Biol.* **3**, 1–11 (2020).

11. Balaban, N. Q. *et al.* Force and focal adhesion assembly: a close relationship studied using elastic micropatterned substrates. *Nat. Cell Biol.* **3**, 466–72 (2001).

12. Malandrino, A., Trepat, X., Kamm, R. D. & Mak, M. Dynamic filopodial forces induce accumulation, damage, and plastic remodeling of 3D extracellular matrices. *PLoS Comput. Biol.* **15**, 1–26 (2019).

13. Colin-York, H. & Fritzsche, M. The future of traction force microscopy. *Curr. Opin. Biomed. Eng.* **5**, 1–5 (2018).

14. Lohela, M. & Werb, Z. Intravital imaging of stromal cell dynamics in tumors. *Curr. Opin. Genet. Dev.* **20**, 72–78 (2010).

15. Malandrino, A., Mak, M., Kamm, R. D. & Moeendarbary, E. Complex mechanics of the heterogeneous extracellular matrix in cancer. *Extrem. Mech. Lett.* **21**, 25–34 (2018).

16. Hazlett, L. *et al.* Epifluorescence-based three-dimensional traction force microscopy. *Sci. Reports 2021 101* **10**, 1–12 (2020).

17. Christiansen, E. M. *et al.* In Silico Labeling: Predicting Fluorescent Labels in Unlabeled Images. *Cell* **173**, 792-803.e19 (2018).

18. Ounkomol, C., Seshamani, S., Maleckar, M. M., Collman, F. & Johnson, G. R. Label-free prediction of three-dimensional fluorescence images from transmitted-light microscopy.

Nat. Methods **15**, 917–920 (2018).

19. Conrad, C. & Gerlich, D. W. Automated microscopy for high-content RNAi screening. *J. Cell Biol.* **188**, 453–461 (2010).

20. Wang, H. *et al.* Deep learning enables cross-modality super-resolution in fluorescence microscopy. *Nat. Methods* **16**, 103–110 (2019).

21. Jemielita, M., Taormina, M. J., Delaurier, A., Kimmel, C. B. & Parthasarathy, R. Comparing phototoxicity during the development of a zebrafish craniofacial bone using confocal and light sheet fluorescence microscopy techniques. *J. Biophotonics* **6**, 920–928 (2013).

22. Dixit, R. & Cyr, R. Cell damage and reactive oxygen species production induced by fluorescence microscopy: Effect on mitosis and guidelines for non-invasive fluorescence microscopy. *Plant J.* **36**, 280–290 (2003).

23. Cole, R. Live-cell imaging: The cell's perspective. *Cell Adhes. Migr.* **8**, 452–459 (2014).

24. Icha, J., Weber, M., Waters, J. C. & Norden, C. Phototoxicity in live fluorescence microscopy, and how to avoid it. *BioEssays* **39**, 1–15 (2017).

25. Hayashida, J., Nishimura, K. & Bise, R. MPM: Joint representation of motion and position map for cell tracking. *Proc. IEEE Comput. Soc. Conf. Comput. Vis. Pattern Recognit.* 3822–3831 (2020). doi:10.1109/CVPR42600.2020.00388

26. Wen, C. *et al.* 3DeeCellTracker, a deep learning-based pipeline for segmenting and tracking cells in 3D time lapse images. *Elife* **10**, e59187 (2021).

27. Moen, E. *et al.* Deep learning for cellular image analysis. *Nat. Methods* **16**, 1233–1246 (2019).

28. Paluch, E. & Heisenberg, C. P. Biology and Physics of Cell Shape Changes in Development. *Curr. Biol.* **19**, R790–R799 (2009).

29. Francou, A. & Anderson, K. V. The Epithelial-to-Mesenchymal Transition in Development and Cancer. *https://doi.org/10.1146/annurev-cancerbio-030518-055425* **4**, 197–220 (2020).

30. Padhi, A. *et al.* Bioenergetics underlying single-cell migration on aligned nanofiber scaffolds. *Am. J. Physiol. - Cell Physiol.* **318**, C476–C485 (2020).

31. Sheets, K., Wang, J., Zhao, W., Kapania, R. & Nain, A. S. Nanonet Force Microscopy for Measuring Cell Forces. *Biophys. J.* **111**, 197–207 (2016).

32. Jana, A. *et al.* Sculpting rupture-free nuclear shapes in fibrous environments. *Adv. Sci.* 2021.10.19.465049 (2022). doi:10.1002/advs.202203011

33. Jana, A. *et al.* Crosshatch nanofiber networks of tunable interfiber spacing induce plasticity in cell migration and cytoskeletal response. *FASEB J.* **33**, fj-201900131R (2019).

34. Clark, A. G. & Vignjevic, D. M. Modes of cancer cell invasion and the role of the microenvironment. *Curr. Opin. Cell Biol.* **36**, 13–22 (2015).

35. Haydont, V., Bernard, B. A. & Fortunel, N. O. Age-related evolutions of the dermis: Clinical signs, fibroblast and extracellular matrix dynamics. *Mechanisms of Ageing and Development* **177**, 150–156 (2019).

36. Glentis, A. *et al.* Cancer-associated fibroblasts induce metalloprotease-independent cancer cell invasion of the basement membrane. *Nat. Commun.* **8**, 1–13 (2017).

37. Taylor, E. N., Hoffman, M. P., Aninwene, G. E. & Gilbert, R. J. Patterns of Intersecting Fiber Arrays Revealed in Whole Muscle with Generalized Q-Space Imaging. *Biophys. J.* **108**, 2740–2749 (2015).

38. Boote, C. *et al.* The Influence of Lamellar Orientation on Corneal Material Behavior: Biomechanical and Structural Changes in an Avian Corneal Disorder. *Invest. Ophthalmol. Vis. Sci.* **52**, 1243–1251 (2011).

39. Weigelin, B., Bakker, G.-J. & Friedl, P. Intravital third harmonic generation microscopy of collective melanoma cell invasion. *IntraVital* **1**, 32–43 (2012).

40. Isola, P., Zhu, J.-Y., Zhou, T. & Efros, A. A. Image-to-image translation with conditional adversarial networks. in *Proceedings of the IEEE conference on computer vision and pattern recognition* 1125–1134 (2017).

41. Mirza, M. & Osindero, S. Conditional generative adversarial nets. *arXiv Prepr. arXiv1411.1784* (2014).

42. Goodfellow, I. J. *et al.* Generative adversarial networks. *arXiv Prepr. arXiv1406.2661* (2014).

43. Lin, T. Y., Goyal, P., Girshick, R., He, K. & Dollar, P. Focal Loss for Dense Object Detection. *IEEE Trans. Pattern Anal. Mach. Intell.* **42**, 318–327 (2020).

44. Tan, P.-N., Steinbach, M. & Kumar, V. *Introduction to data mining*. (Pearson Education India, 2016).

45. Jana, A. *et al.* Sculpting Rupture-Free Nuclear Shapes in Fibrous Environments. *Adv. Sci.* **9**, 2203011 (2022).

46. Fu, J. *et al.* Mechanical regulation of cell function with geometrically modulated elastomeric substrates. *Nat. Methods* **7**, 733–736 (2010).

47. Han, S. J., Oak, Y., Groisman, A. & Danuser, G. Traction microscopy to identify force modulation in subresolution adhesions. *Nat. Methods* **12**, 653–656 (2015).

48. Han, S. J., Bielawski, K. S., Ting, L. H., Rodriguez, M. L. & Sniadecki, N. J. Decoupling Substrate Stiffness, Spread Area, and Micropost Density: A Close Spatial Relationship between Traction Forces and Focal Adhesions. *Biophys. J.* **103**, 640–648 (2012).

49. Tan, J. L. *et al.* Cells lying on a bed of microneedles: An approach to isolate mechanical force. *Proc. Natl. Acad. Sci. U. S. A.* **100**, 1484–1489 (2003).

50. Steinwachs, J. *et al.* Three-dimensional force microscopy of cells in biopolymer networks. *Nat. Methods* **13**, 171–176 (2016).

51. Lekka, M., Gnanachandran, K., Kubiak, A., Zieliński, T. & Zemła, J. Traction force microscopy – Measuring the forces exerted by cells. *Micron* **150**, (2021).

52. Xue, X., Hong, X., Li, Z., Deng, C. X. & Fu, J. Acoustic tweezing cytometry enhances osteogenesis of human mesenchymal stem cells through cytoskeletal contractility and YAP activation. *Biomaterials* **134**, 22–30 (2017).

53. Tijore, A. *et al.* Role of Cytoskeletal Tension in the Induction of Cardiomyogenic

Differentiation in Micropatterned Human Mesenchymal Stem Cell. *Adv. Healthc. Mater.* **4**, 1399–1407 (2015).

54. Engler, A. J., Sen, S., Sweeney, H. L. & Discher, D. E. Matrix Elasticity Directs Stem Cell Lineage Specification. *Cell* **126**, 677–689 (2006).

55. Khetan, S. *et al.* Degradation-mediated cellular traction directs stem cell fate in covalently crosslinked three-dimensional hydrogels. *Nat. Mater.* **12**, 458–465 (2013).

56. Abuhattum, S., Gefen, A. & Weihs, D. Ratio of total traction force to projected cell area is preserved in differentiating adipocytes. *Integr. Biol. (United Kingdom)* **7**, 1212–1217 (2015).

57. Lautscham, L. A. *et al.* Migration in Confined 3D Environments Is Determined by a Combination of Adhesiveness, Nuclear Volume, Contractility, and Cell Stiffness. *Biophys. J.* **109**, 900–913 (2015).

58. Kraning-Rush, C. M., Carey, S. P., Califano, J. P., Smith, B. N. & Reinhart-King, C. A. The role of the cytoskeleton in cellular force generation in 2D and 3D environments. *Phys. Biol.* **8**, (2011).

59. Tang, X., Tofangchi, A., Anand, S. V. & Saif, T. A. A Novel Cell Traction Force Microscopy to Study Multi-Cellular System. *PLoS Comput. Biol.* **10**, (2014).

60. Traction Force Microscopy by Deep Learning Y.L. Wang and Y.-C. Lin Keywords: mechanobiology, traction forces, machine learning 1. (2020).

61. Nain, A. S., Sitti, M., Jacobson, A., Kowalewski, T. & Amon, C. Dry spinning based spinneret based tunable engineered parameters (STEP) technique for controlled and aligned deposition of polymeric nanofibers. *Macromol. Rapid Commun.* **30**, (2009).

62. Wang, J. & Nain, A. S. Suspended micro/nanofiber hierarchical biological scaffolds fabricated using non-electrospinning STEP technique. *Langmuir* **30**, (2014).

63. Nain, A. S. & Wang, J. Polymeric nanofibers: isodiametric design space and methodology for depositing aligned nanofiber arrays in single and multiple layers. *Polym. J.* **45**, 695–700 (2013).

64. De Borst, R., Crisfield, M. A., Remmers, J. J. C. & Verhoosel, C. V. *Nonlinear finite element analysis of solids and structures*. (John Wiley & Sons, 2012).

65. Schwarz, U. S. & Soiné, J. R. D. Traction force microscopy on soft elastic substrates: A guide to recent computational advances. *Biochim. Biophys. Acta* **1853**, 3095–3104 (2015).

66. Kass, M., Witkin, A. & Terzopoulos, D. Snakes: Active contour models. *Int. J. Comput. Vis.* **1**, 321–331 (1988).

67. Cohen, L. D. On active contour models and balloons. *CVGIP Image Underst.* **53**, 211–218 (1991).

68. Nocedal, J. & Wright, S. J. *Numerical Optimization*. (Springer, New York, NY, 2006).

69. Oberai, A. A., Gokhale, N. H. & Feijóo, G. R. Solution of inverse problems in elasticity imaging using the adjoint method. *Inverse Probl.* **19**, 297 (2003).

70. Song, D., Hugenberg, N. & Oberai, A. A. Three-dimensional traction microscopy with a fiber-based constitutive model. *Comput. Methods Appl. Mech. Eng.* **357**, 112579 (2019).

71. Song, D. *et al.* Recovery of tractions exerted by single cells in three-dimensional nonlinear matrices. *J. Biomech. Eng.* **142**, 81012 (2020).